A Misalignment-Tolerant Autonomous Wireless Power Transfer System for Battery Charging Based on Detuning Control

Lihao Wu, Bo Zhang, *Fellow, IEEE*, and Yanwei Jiang, *Member, IEEE*

***Abstract*—This article proposed an autonomous wireless power transfer system with misalignment tolerance and improved control degree of freedom based on detuning control for battery charging, in which the outputs can be regulated continuously and smoothly without additional dc–dc converters while maintaining soft-switching or zero-phase-angle operation of the inverter. Theoretical analysis shows that constant current (CC) or constant voltage (CV) independent of coupling coefficient and load can be achieved without information exchange between transmitter and receiver, which eliminates wireless communication. Furthermore, when the detuning ratio is controlled to be constant, a transfer efficiency insensitive to the variation of the coupling coefficient can be obtained. A prototype with a 6-A charging current and a 36-V charging voltage is built to support the feasibility of the proposed method. Experimental results demonstrate that within the coupling coefficient range of 0.283–0.456, CC and CV with transfer efficiency greater than 91.5% can be achieved.**

***Index Terms*—Autonomous system, battery charging, detuning control, misalignment tolerance, wireless power transfer (WPT).**

I. Introduction

WIRELESS power transfer (WPT) can deliver power without any physical contact, it has been applied to various fields, especially smartphones, electric vehicles, and automated guided vehicles [1], [2], [3]. Currently, the most widely used WPT system is based on magnetic field coupling due to its safety and reliability. In general, the transmitter and receiver must be aligned to achieve the best performance of a magnetic-coupled WPT system. However, misalignment between transmitter and receiver in a WPT system is inevitable. For example, the misalignment may occur because of an imprecise parking position of the vehicles or inaccurate placement of mobile phones. Therefore, it is essential to design a misalignment-tolerant WPT system. Besides, for applications such as smartphones or vehicles, batteries are usually used to store energy. The constant current/constant voltage (CC/CV) charging mode is typically applied for the battery to improve battery life. In this charging mode, the battery is equivalent to a variable resistance load, and its value depends on the battery's state of charge. Thus, it is also necessary to consider changes in load during the design process.

For a typical magnetic coupled WPT system, the operating frequency is dependent on the frequency of the external power supply and is normally set equal to the resonant frequency of the transmitter and receiver. Essentially, it can be considered a nonautonomous system. In this type of system, the methods for achieving CC/CV outputs under misalignment conditions can be categorized into two groups: 1) open-loop control and 2) closed-loop control. The open-loop control mainly involves hybrid compensation topology design and coil design. According to reported studies, a single type of compensation topology, including basic compensation topology [4], [5] or higher-order compensation topology [6], [7], can already achieve CC/CV outputs. However, for these single types of compensation topology, the outputs are related to the coupling coefficient. That is, when the misalignment occurs, the constant output characteristic will be destroyed. For this reason, the hybrid compensation topology [8], [9], which connects the input (or output) of different types of topologies in series or parallel, is proposed to maintain a constant output in case of misalignment. Unfortunately, the control accuracy is limited, and its output fluctuates are still significant, especially for the wide variation range of the coupling coefficient. The design of coupling coils is another method to improve the misalignment tolerance, including coil arrays [10] and three-dimensional coils [11]. However, these methods can only provide a quasi-constant output and the structure of the coupling coil is complex.

Accurate CC and CV outputs can be obtained by the closed-loop control method, which can be further classified as transmitter-side and receiving-side control. The receiver-side control methods often require additional circuits (such as dc–dc converters [12], [13] and active rectifiers [14], [15]) to regulate the outputs, which violates the compact and lightweight requirements of the receiver. Therefore, the transmitter-side control methods are fully considered in this article. The one type of transmitter-side control is based on a dc–dc converter [16], which increases the device cost and power losses. Another type is

Manuscript received 8 October 2023; revised 30 November 2023; accepted 15 December 2023. Date of publication 19 December 2023; date of current version 26 January 2024. This work was supported by the Key Program of the National Natural Science Foundation of China under Grant 52130705. Recommended for publication by Associate Editor K. B. Park. *(Corresponding author: Bo Zhang.)*

Lihao Wu and Bo Zhang are with the School of Electric Power, South China University of Technology, Guangzhou 510640, China (e-mail: wulh20239003@scut.edu.cn; epbzhang@scut.edu.cn).

Yanwei Jiang is with the College of Electrical Engineering and Automation, Fuzhou University, Fuzhou 350000, China (e-mail: jiang_yanwei@fzu.edu.cn).

Color versions of one or more figures in this article are available at https://doi.org/10.1109/TPEL.2023.3344509.

Digital Object Identifier 10.1109/TPEL.2023.3344509

executed by a single-stage inverter. When acting on the inverter, phase shift control [17], [18], frequency control [19], and pulse frequency modulation [20] are often used to adjust the outputs when operation conditions change. However, real-time wireless communication is usually required to feedback information from the receiving side. The performance of the WPT system will be inevitably affected due to communication delay problems or even interruption issues. To get rid of the dependence on communication, parameter identification methods have been proposed [21], which utilize the transmitter-side electrical information to estimate mutual inductance and load resistance, thereby achieving control of output power. However, the accuracy of estimation is sensitive to circuit parameter variations, and some of them belong to an offline estimation method [22].

Apart from the traditional nonautonomous WPT systems, autonomous WPT systems have also been developed due to their inherent misalignment-tolerant characteristics [23], [24], [25], [26], [27], [28]. The parity-time (PT) symmetric WPT is a typical autonomous WPT system. For the PT-symmetric system, the matched resonance frequency is needed, and the corresponding operation depends on the internal electrical state of the system. In [23] and [24], it has been revealed that an inherently constant efficiency and power against the variation of the coupling coefficient can be achieved without dual-side communication. However, the change in the load resistance is not considered, which cannot be applied to battery charging. To cope with load changes, a dc–dc converter is added at the front end of the inverter [26], but the cascaded converter will also cause additional loss and cost. Recently, phase shift control [27] and pulse frequency modulation [28] have been applied to PT-symmetric WPT systems to regulate the output power with a single-stage inverter. However, the phase shift control suffers from hard switching issues, which causes high switching loss. Although soft switching can be realized by using pulse frequency modulation, the output power cannot be continuously adjusted, resulting in a large output ripple.

To address the abovementioned issues, this article proposes a misalignment-tolerant autonomous wireless charging system based on detuning control, which is different from the existing control ideas that require resonance matching. By controlling the deviation ratio between the resonant frequency of the transmitter and receiver and the operating frequency of the system (i.e., detuning ratio), the degree of control freedom of the system can be significantly improved. The advantages of the proposed system are summarized as follows.

1) By adjusting the detuning ratio, the output power can be continuously and smoothly regulated using a single-stage inverter, and no extra dc–dc converters are added on both sides.
2) CC and CV outputs independent of coupling coefficient and load can be achieved while maintaining soft-switching or zero-phase-angle (ZPA) operation.
3) When the detuning ratio is controlled to be constant, a constant transfer efficiency against the variation of the coupling coefficient can be obtained. Besides, the transfer efficiency can be improved by increasing the detuning ratio.

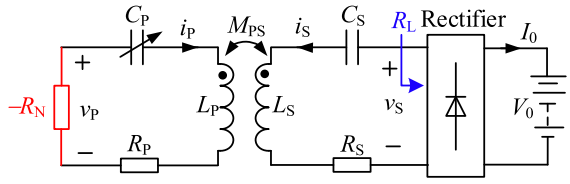

Fig. 1. Equivalent circuit of the proposed autonomous WPT system.

4) Transmitter-side control is used, which eliminates wireless communication for real-time output regulation.

II. Theoretical Modeling and Analysis

A. System Modeling

The equivalent circuit of the proposed autonomous WPT system is shown in Fig. 1, where the transmitter and receiver are coupled together by two coils L_P and L_S with mutual inductance M_{PS}. In contrast to standard nonautonomous WPT schemes, the transmitter contains a negative resistor $-R_N$ (with the current direction opposite that of a normal resistor for a given applied voltage). The power of the proposed system is instead injected by the negative resistor rather than a high-frequency source at a fixed frequency. C_P and C_S are the compensation capacitors of the transmitter and receiver, respectively, where C_P is a switch-controlled capacitor (SCC). R_L is the equivalent ac load resistance of the rectifier. i_P and i_S represent the currents of transmitting and receiving coils, respectively. v_P is the voltage across the negative resistor and v_S is the input voltage of the rectifier. The dc charging voltage and the dc charging current are denoted as V_o and I_o, respectively.

Due to the bandpass filter feature of the series resonant compensation network, only the fundamental components of voltage and current are considered. v_P, v_S, i_P, and i_S can be easily expressed in terms of phasors $\dot{V}_P$, $\dot{V}_S$, $\dot{I}_P$, and $\dot{I}_S$, respectively. According to the circuit theory, the system can be expressed as

$$\begin{bmatrix} \frac{-R_N+R_P}{L_P}+j\left(\frac{\omega^2-\omega_P^2}{\omega}\right) & j\omega k_{PS}\sqrt{\frac{L_S}{L_P}} \\ j\omega k_{PS}\sqrt{\frac{L_P}{L_S}} & \frac{R_L+R_S}{L_S}+j\left(\frac{\omega^2-\omega_S^2}{\omega}\right) \end{bmatrix} \begin{bmatrix} \dot{I}_P \\ \dot{I}_S \end{bmatrix} = 0 \tag{1}$$

where $k_{PS} = M_{PS}/\sqrt{L_P L_S}$ is the coupling coefficient between coils. ω is the operating angular frequency of the system, and $\omega_P = 1/\sqrt{L_P C_P}$ and $\omega_S = 1/\sqrt{L_S C_S}$ are the natural frequencies of the transmitter and receiver, respectively.

B. Analysis Solutions of Operating Frequency

Equation (1) is a homogeneous linear equation for current $\dot{I}_P$ and $\dot{I}_S$. According to the theorem of linear algebra, homogeneous linear equations have nontrivial solutions only when the determinant of the corresponding coefficient matrix is equal to zero. When the system is operating normally, the current must not be equal to zero. Therefore, the determinant of (1) should be equal to zero to obtain a steady-state operation frequency

solution, i.e.,

$$\begin{cases} \left(\frac{\omega^2-\omega_{\mathrm{P}}^2}{\omega}\right)\frac{R_{\mathrm{L}}+R_{\mathrm{S}}}{L_{\mathrm{S}}}+\left(\frac{\omega^2-\omega_{\mathrm{S}}^2}{\omega}\right)\frac{-R_{\mathrm{N}}+R_{\mathrm{P}}}{L_{\mathrm{P}}}=0 \\ \frac{-R_{\mathrm{N}}+R_{\mathrm{P}}}{L_{\mathrm{P}}}\frac{R_{\mathrm{L}}+R_{\mathrm{S}}}{L_{\mathrm{S}}}-\left(\frac{\omega^2-\omega_{\mathrm{P}}^2}{\omega}\right)\left(\frac{\omega^2-\omega_{\mathrm{S}}^2}{\omega}\right)+\omega^2k_{\mathrm{PS}}^2=0. \end{cases} \tag{2}$$

Define the detuning ratio as

$$\beta=\frac{\omega^2-\omega_{\mathrm{P}}^2}{\omega^2-\omega_{\mathrm{S}}^2}. \tag{3}$$

Submitting (3) into (2), (2) can be further simplified as

$$\begin{cases} \frac{-R_{\mathrm{N}}+R_{\mathrm{P}}}{L_{\mathrm{P}}}=-\frac{R_{\mathrm{L}}+R_{\mathrm{S}}}{L_{\mathrm{S}}}\beta \\ \left(\beta-k_{\mathrm{PS}}^2\right)\omega^4+\left[\beta\left(\frac{R_{\mathrm{L}}+R_{\mathrm{S}}}{L_{\mathrm{S}}}\right)^2-2\beta\omega_{\mathrm{S}}^2\right]\omega^2+\beta\omega_{\mathrm{S}}^4=0. \end{cases} \tag{4}$$

In practice, the system can only operate at pure real operating angular frequencies, and complex operating frequencies cannot be generated in actual systems. Thus, it is necessary to derive the steady-state solution with a purely real ω. From (4), the real solutions of ω can be deduced as

$$\omega=\omega_{\mathrm{H}}=\omega_{\mathrm{S}}\sqrt{\frac{[2\beta-\beta\gamma^2]+\sqrt{[2\beta-\beta\gamma^2]^2-4\left(\beta^2-\beta k_{\mathrm{PS}}^2\right)}}{2\left(\beta-k_{\mathrm{PS}}^2\right)}},\ k_{\mathrm{PS}}\geq k_{\mathrm{C}} \tag{5a}$$

$$\omega=\omega_{\mathrm{L}}=\omega_{\mathrm{S}}\sqrt{\frac{[2\beta-\beta\gamma^2]-\sqrt{[2\beta-\beta\gamma^2]^2-4\left(\beta^2-\beta k_{\mathrm{PS}}^2\right)}}{2\left(\beta-k_{\mathrm{PS}}^2\right)}},\ k_{\mathrm{PS}}\geq k_{\mathrm{C}} \tag{5b}$$

where ω_{H} denotes the high-frequency branch, and ω_{L} represents the low-frequency branch, and

$$k_{\mathrm{C}}=\sqrt{\beta}\sqrt{\frac{\gamma^2-\gamma^4}{4}},\ \gamma=\frac{R_{\mathrm{L}}+R_{\mathrm{S}}}{\omega_{\mathrm{S}}L_{\mathrm{S}}}. \tag{6}$$

The k_{C} is the critical condition for the occurrence of saddle-node bifurcation in a system [29], which corresponds to the boundary of strong coupling and weak coupling regions in the WPT system. It can be observed that k_{C} decreases with the decrease of β and the increase of ω_{S} and L_{S}. By reducing the detuning ratio or increasing the self-inductance and natural frequency of the receiver, the operation range with stable transmission characteristics can be extended. ω_{H} and ω_{L} are the eigenfrequencies of the system, which correspond to the two bifurcation solutions of the system in a strongly coupled region (i.e., $k_{\mathrm{PS}}\geq k_{\mathrm{C}}$). When the system oscillates at ω_{H} or ω_{L}, ZPA operation can always be maintained under different coupling coefficients, load resistances, and detuning ratios. It should be emphasized that, according to the abovementioned analysis, $\omega=\omega_{\mathrm{H}}$ (or $\omega=\omega_{\mathrm{L}}$) will automatically be satisfied if the system input power is provided by a negative resistor when $k_{\mathrm{PS}}\geq k_{\mathrm{C}}$.

C. Analysis of Transmission Characteristics

According to (1), the current ratio can be deduced

$$\frac{I_{\mathrm{S}}}{I_{\mathrm{P}}}=\left|\frac{\dot{I}_{\mathrm{S}}}{\dot{I}_{\mathrm{P}}}\right|=\sqrt{\frac{\left(\frac{\omega^2-\omega_{\mathrm{P}}^2}{\omega}\right)^2+\left(\frac{-R_{\mathrm{N}}+R_{\mathrm{P}}}{L_{\mathrm{P}}}\right)^2}{\omega^2k_{\mathrm{PS}}^2L_{\mathrm{S}}/L_{\mathrm{P}}}}. \tag{7}$$

By inserting (2) and (3) into (7), the current ratio can be expressed as

$$\begin{aligned}\frac{I_{\mathrm{S}}}{I_{\mathrm{P}}}=\left|\frac{\dot{I}_{\mathrm{S}}}{\dot{I}_{\mathrm{P}}}\right|&=\sqrt{\frac{\beta^2\left[\left(\omega^2-\omega_{\mathrm{S}}^2\right)/\omega\right]^2+\beta^2\left[\left(R_{\mathrm{L}}+R_{\mathrm{S}}\right)/L_{\mathrm{S}}\right]^2}{\omega^2k_{\mathrm{PS}}^2L_{\mathrm{S}}/L_{\mathrm{P}}}} \\ &=\sqrt{\frac{\beta^2\left[\left(\omega^2-\omega_{\mathrm{S}}^2\right)/\omega\right]^2+\beta^2\left[\left(R_{\mathrm{L}}+R_{\mathrm{S}}\right)/L_{\mathrm{S}}\right]^2}{\left[\beta\left[\left(R_{\mathrm{L}}+R_{\mathrm{S}}\right)/L_{\mathrm{S}}\right]^2+\beta\left[\left(\omega^2-\omega_{\mathrm{S}}^2\right)/\omega\right]^2\right]\frac{L_{\mathrm{S}}}{L_{\mathrm{P}}}}} \\ &=\sqrt{\beta}\sqrt{\frac{L_{\mathrm{P}}}{L_{\mathrm{S}}}}.\end{aligned} \tag{8}$$

From (8), it can be found that the current ratio is relative to the ratio of L_{P} and L_{S} and the detuning ratio β. Once these parameters are fixed, a constant current ratio independent of the coupling coefficient and load can be achieved. Furthermore, the current ratio can be easily regulated by adjusting the detuning ratio, which significantly increases the degree of control freedom.

Using (2) and (8), the voltage ratio of the proposed system can be derived as

$$\left.\begin{array}{l}\frac{R_{\mathrm{L}}+R_{\mathrm{S}}}{L_{\mathrm{S}}}\beta=\frac{R_{\mathrm{N}}-R_{\mathrm{P}}}{L_{\mathrm{P}}} \\ V_{\mathrm{S}}=R_{\mathrm{L}}I_{\mathrm{S}},\ V_{\mathrm{P}}=R_{\mathrm{N}}I_{\mathrm{P}} \\ \frac{I_{\mathrm{P}}}{I_{\mathrm{S}}}=\sqrt{\frac{1}{\beta}}\sqrt{\frac{L_{\mathrm{S}}}{L_{\mathrm{P}}}}\end{array}\right\}$$

$$\Rightarrow\frac{V_{\mathrm{S}}}{V_{\mathrm{P}}}=\frac{1}{\sqrt{\beta}}\sqrt{\frac{L_{\mathrm{S}}}{L_{\mathrm{P}}}}-\frac{I_{\mathrm{P}}}{V_{\mathrm{P}}}\left(\sqrt{\frac{L_{\mathrm{S}}}{L_{\mathrm{P}}}}\frac{R_{\mathrm{P}}}{\sqrt{\beta}}+R_{\mathrm{S}}\sqrt{\beta}\sqrt{\frac{L_{\mathrm{P}}}{L_{\mathrm{S}}}}\right). \tag{9}$$

Ignoring the internal resistance of the coil (i.e., R_{P}, $R_{\mathrm{S}}\approx 0$), the voltage gain can be further reduced to

$$\frac{V_{\mathrm{S}}}{V_{\mathrm{P}}}=\frac{1}{\sqrt{\beta}}\sqrt{\frac{L_{\mathrm{S}}}{L_{\mathrm{P}}}}. \tag{10}$$

It can be seen from (10) that a constant voltage ratio independent of coupling coefficient and load can be also obtained. Besides, according to (9), an accurate voltage ratio can be calculated only by sampling the detuning ratio β and the transmitting current I_{P}.

Based on (8) and (9), the transfer efficiency and output power can be given as

$$\eta_{\mathrm{T}}=\frac{I_{\mathrm{S}}^2R_{\mathrm{L}}}{I_{\mathrm{P}}^2R_{\mathrm{P}}+I_{\mathrm{S}}^2R_{\mathrm{S}}+I_{\mathrm{S}}^2R_{\mathrm{L}}}=\frac{R_{\mathrm{L}}}{\frac{1}{\beta}\frac{L_{\mathrm{S}}}{L_{\mathrm{P}}}R_{\mathrm{P}}+R_{\mathrm{S}}+R_{\mathrm{L}}} \tag{11}$$

$$\begin{aligned}P_{\mathrm{T}}&=\frac{V_{\mathrm{S}}^2}{R_{\mathrm{L}}} \\ &=\frac{\beta R_{\mathrm{L}}V_{\mathrm{P}}^2}{\frac{L_{\mathrm{P}}}{L_{\mathrm{S}}}\left(R_{\mathrm{L}}+R_{\mathrm{S}}\right)^2\beta^2+2R_{\mathrm{P}}\left(R_{\mathrm{L}}+R_{\mathrm{S}}\right)\beta+\frac{L_{\mathrm{S}}}{L_{\mathrm{P}}}R_{\mathrm{P}}^2}.\end{aligned} \tag{12}$$

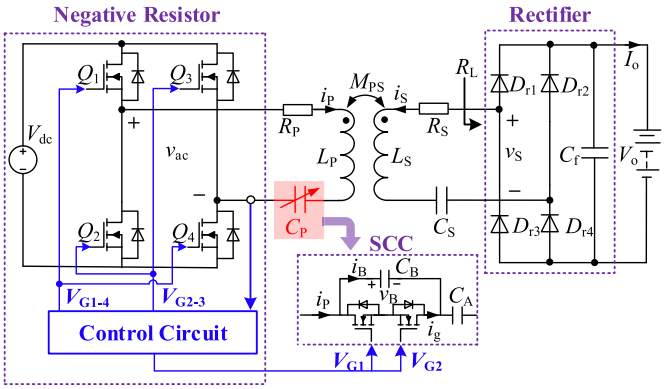

Fig. 2. Overall circuit diagram of the proposed autonomous WPT system.

From (11) and (12), it can be observed that the transfer efficiency and output power are insensitive to the coupling coefficient, which indicates that constant transfer efficiency and output power can be maintained when misalignment occurs. Besides, according to (11), the transfer efficiency can be improved by increasing the detuning ratio. In exiting autonomous WPT systems, the output power can only be regulated by adjusting V_{P} using phase shift control [27] or pulse frequency modulation [28], which destroys the soft-switching or suffers a large output voltage ripple. Inspecting (12), the output power of the proposed WPT system can be regulated by changing the detuning ratio β when V_{P} is fixed. The advantage is that continuous and smooth adjustable outputs can be achieved while maintaining soft-switching operation.

III. Implementation and Control

A. Structure of the Proposed System

Based on Fig. 1, the overall circuit diagram of the proposed autonomous WPT system is shown in Fig. 2. The topology of the main circuit is composed of an H-bridge inverter that behaves like a resistor of value $-R_{\mathrm{N}}$, a series–series (SS) type compensation network, and a bridge diode rectifier. The transmitting-side compensation capacitor C_{P} is replaced by a SCC. Its equivalent capacitance varies adaptively according to the required detuning ratio.

1) Implementation of Negative Resistor: The negative resistor is a type of component that corresponds to the positive resistor. The positive resistor has a positive resistance value and consumes power, making it a passive component. The negative resistor has a negative resistance value and is an active component that outputs power. For a given voltage, the direction of current flowing through a negative resistor is always opposite to that of a positive resistor [30]. According to Ohm's law, the current flowing through a positive resistor flows from high potential to low potential, while the current flowing through a negative resistor flows from low potential to high potential. In the case of sinusoidal ac signals, the ac current flowing through the negative resistor always maintains a reverse direction with the ac voltage across it, i.e., when an associated reference direction is chosen, the phase difference between ac voltage across the negative resistor and the ac current flowing through it remains 180° for each cycle.

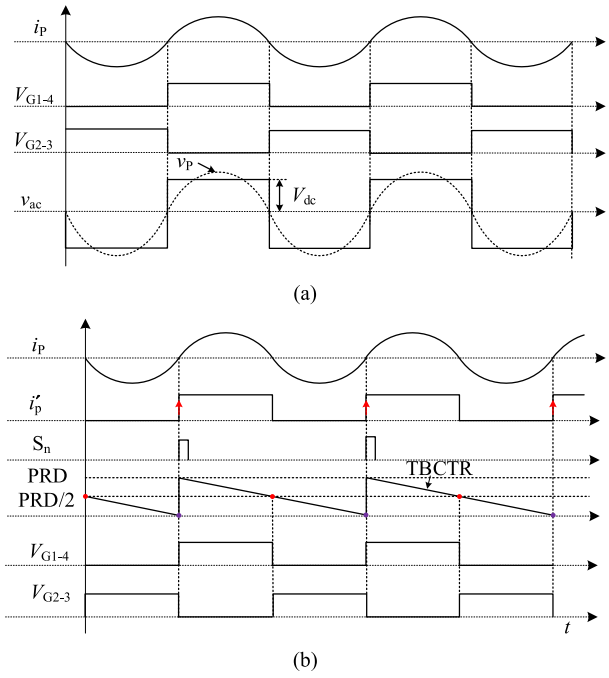

Fig. 3. Details of (a) operating waveforms of the inverter and (b) generation process of the driver signals.

In this article, an H-bridge inverter is used to construct a negative resistor. According to the definition of the negative resistor, when the phase difference between the fundamental component of the inverter voltage and its output current is always maintained at 180°, the output of the inverter can be equivalent to a negative resistance (only the fundamental components of voltage and current need to be considered due to the bandpass filter feature of the series resonant compensation network). Because the nonassociated reference direction, as shown in Fig. 2 is selected, the phase difference between the inverter output voltage and current should be controlled to zero.

Fig. 3(a) shows the operating waveforms of the inverter, where the duty cycle of the driving signal $V_{\mathrm{G1\text{-}4}}$ for MOSFET Q_1, Q_4 and driving signal $V_{\mathrm{G2\text{-}3}}$ for Q_2, Q_3 are set to be 50% without considering the dead time. As shown in Fig. 3(a), $V_{\mathrm{G1\text{-}4}}$ and $V_{\mathrm{G2\text{-}3}}$ complement each other, and the rising edge of the drive signal $V_{\mathrm{G1\text{-}4}}$ is synchronized with the zero-crossing point of the current i_{P}. Additionally, it can be noted that controlled by $V_{\mathrm{G1\text{-}4}}$ and $V_{\mathrm{G2\text{-}3}}$, the zero-phase angle of the input voltage and current can be achieved (i.e., the negative resistor is realized), which allows for a minimum volt-ampere rating of the inverter and helps maintain the soft switching.

Fig. 3(b) shows the generation process of the driving signals based on the phase synchronization method [27]. The drive signals $V_{\mathrm{G1\text{-}4}}$ and $V_{\mathrm{G2\text{-}3}}$ are, respectively, generated by A and B channels of an enhanced pulse width modulation (i.e., ePWM1A and ePWM1B) module in DSP. As shown in Fig. 3(b), the time-base counter (TBCTR) of the PWM module is configured to operate in the down-count mode. In down-count mode, the TBCTR starts from the period (PRD) value and decreases until

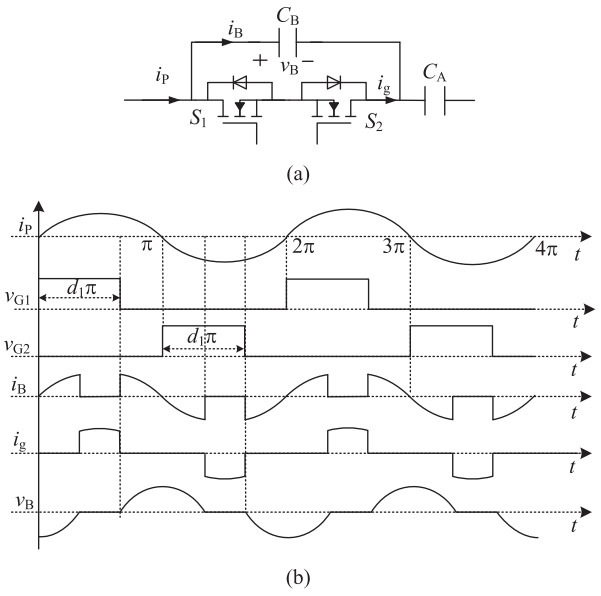

Fig. 4. (a) Structure and (b) operating waveforms of the SCC.

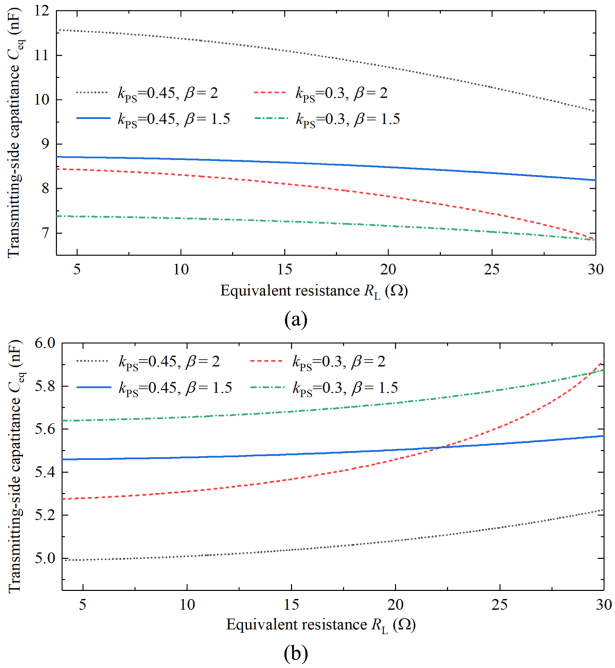

Fig. 5. Required compensation transmitting-side capacitance under (a) $\omega = \omega_H$ and (b) $\omega = \omega_L$.

it reaches zero, when it reaches zero, the TBCTR is reset to the PRD value and it begins to decrease once again. When the TBCTR is equal to zero, $V_{G1\text{-}4}$ is forced to be a high level, and $V_{G2\text{-}3}$ is forced to be a low level. When TBCTR is equal to half of the period (PRD/2), $V_{G1\text{-}4}$ is forced to be a low level, and $V_{G2\text{-}3}$ is forced to be a high level (where PRD $= T_S$ / T_{CLK} and $T_S = 2\pi$ / ω is the operating period captured in real-time by CAP module of DSP and T_{CLK} represents the time required for TBCTR to decrease by 1). In order to control the synchronization of the rising edge of $V_{G1\text{-}4}$ with the zero-crossing point of i_P, the current i_P is sensed and passed through a zero-crossing comparator to generate the square wave i'_P, which is in phase with i_P. Then, the rising edge of i'_P is captured by the CAP module of DSP. When the rising edge of i'_P arrives, a synchronization pulse of the ePWM1 module (S_n) is generated, and TBCTR is updated to zero immediately. Besides, it should be noted that the system will be initially set to operate at $\omega = \omega_{init}$ because there is no current in the transmitter at the beginning. During the start-up stage, fixed-frequency driving signals are produced directly by DSP and the system works in a forced oscillation mode. After creating the i_P, the driving signals are generated according to Fig. 3(b) so that the inverter can behave as a negative resistor.

2) Implementation of Switch-Controlled Capacitor: To adjust the detuning ratio, a full-wave SCC [31] is used as compensation capacitor C_P in this article. Fig. 4(a) shows the structure of the SCC, which is composed of a parallel capacitor C_B and a bidirectional switch (consisting of two drain-to-drain connected MOSFETS S_1 and S_2), and a series capacitor C_A. Because the charge state of C_B can be controlled by the bidirectional switch, the equivalent capacitance of the C_P can be continuously modulated by controlling the PWM signal, thereby achieving adjustment of the detuning ratio.

The operation waveforms of SCC are presented in Fig. 4(b). As shown in Fig. 4(b), S_1 is turned ON when i_P commutates from negative to positive while S_2 is turned ON when i_P commutates from positive to negative. According to Fig. 4, the equivalent capacitance C_{eq} can be derived as follows [31]:

$$C_P = C_{eq} = \frac{\pi C_A C_B}{\pi (C_B + 2C_A) - (2\alpha - \sin 2\alpha) C_A} \tag{13}$$

where $\alpha = d_1\pi$ is a conduction angle and d_1 ($0.5 \le d_1 \le 1$) is the duty cycle of S_1 and S_2.

By submitting (5) into (3), the required compensation transmitting-side capacitance (i.e., C_{eq}) under different load resistances and coupling coefficients can be obtained, as shown in Fig. 5. It can be found in Fig. 5(a) that when $\omega = \omega_H$, C_{eq} is positively correlated with coupling coefficient and negatively correlated with load resistance. In addition, according to (3), it can be known that C_{eq} increases as the detuning ratio increases. From Fig. 5(b), it can be observed that the changing trend of C_{eq} under $\omega = \omega_L$ is opposite to that under $\omega = \omega_H$. In this design, based on (11), the detuning ratio is set to be greater than 1 to improve the transfer efficiency. In this case, C_{eq} under $\omega = \omega_L$ is always smaller than that under $\omega = \omega_H$. Therefore, by submitting the maximum k_{PS} and β, and the minimum R_L into (5a) and (3), the required maximum equivalent capacitance of SCC (i.e., C_{eq_max}) can be obtained. Similarly, submitting the maximum k_{PS} and β, and the minimum R_L into (5b) and (3), the required minimum equivalent capacitance of SCC (i.e., C_{eq_min}) can be deduced. Combining (13) and $C_{eq\_min} \le C_{eq} \le C_{eq\_max}$, the range of the C_A and C_B can be obtained as follows:

$$\begin{cases} C_A \ge C_{eq\_max} \\ C_B \le \frac{C_A C_{eq\_min}}{C_A - C_{eq\_min}}. \end{cases} \tag{14}$$

B. Control Scheme of CC/CV Charging Mode

Considering the fundamental component of voltage and current, the relationship between the input and output of the H-bridge inverter and rectifier, as shown in Fig. 2, can be given as [5]

$$\begin{cases} V_{\mathrm{P}} = 2\sqrt{2}V_{\mathrm{dc}}/\pi \\ I_{\mathrm{S}} = \pi\sqrt{2}I_{\mathrm{o}}/4, V_{\mathrm{S}} = 2\sqrt{2}V_{\mathrm{o}}/\pi \\ R_{\mathrm{L}} = 8R_{\mathrm{B}}/\pi^2 \end{cases} \tag{15}$$

where V_{dc} is the dc input voltage, and $R_{\mathrm{B}} = V_{\mathrm{o}}/I_{\mathrm{o}}$ is the equivalent resistance of the battery.

According to (8), (9), and (15), the dc charging current and voltage can be derived

$$I_{\mathrm{o}} = \frac{2\sqrt{2\beta}I_{\mathrm{P}}}{\pi}\sqrt{\frac{L_{\mathrm{P}}}{L_{\mathrm{S}}}} \tag{16}$$

$$V_{\mathrm{o}} = \frac{V_{\mathrm{dc}}}{\sqrt{\beta}}\sqrt{\frac{L_{\mathrm{S}}}{L_{\mathrm{P}}}} - I_{\mathrm{P}}\frac{\sqrt{2}\pi}{4}\left(\sqrt{\frac{L_{\mathrm{S}}}{L_{\mathrm{P}}}}\frac{R_{\mathrm{P}}}{\sqrt{\beta}} + R_{\mathrm{S}}\sqrt{\beta}\sqrt{\frac{L_{\mathrm{P}}}{L_{\mathrm{S}}}}\right). \tag{17}$$

From (16) and (17), it can be found that the constant charging current and voltage can be obtained when the detuning ratio β satisfies

$$\beta = \beta_{\mathrm{Ref\_CC}} = \frac{I_{\mathrm{o\_Ref}}^2\pi^2 L_{\mathrm{S}}}{8I_{\mathrm{P}}^2 L_{\mathrm{P}}} \tag{18}$$

$$\beta = \beta_{\mathrm{Ref\_CV}} = \left[\frac{-\sqrt{2}\pi V_{0\_\mathrm{Ref}}/4 + A}{2I_{\mathrm{P}}R_{\mathrm{S}}\sqrt{L_{\mathrm{P}}/L_{\mathrm{S}}}}\right]^2 \tag{19}$$

where $I_{\mathrm{o\_Ref}}$ and $V_{\mathrm{o\_Ref}}$ are the rated dc charging current and voltage, respectively, and

$$A = \sqrt{\left(\frac{\sqrt{2}\pi V_{0\_\mathrm{Ref}}}{4}\right)^2 - 4\left(I_{\mathrm{P}}^2 R_{\mathrm{S}}R_{\mathrm{P}} - \frac{I_{\mathrm{P}}R_{\mathrm{S}}2\sqrt{2}V_{\mathrm{dc}}}{\pi}\right)}. \tag{20}$$

By adjusting the detuning ratio in real time to equal the required value, the constant charging current and voltage can be realized when misalignment occurs or load resistance changes. Fig. 6(a) and (b) shows the control block diagram of CC and CV charging modes. As shown in Fig. 6, a proportional-integral (PI) double closed-loop is used in CC mode and CV mode. The output of the inner loop is the required detuning ratio of CC mode and CV mode (i.e., $\beta_{\mathrm{Ref\_CC}}$ and $\beta_{\mathrm{Ref\_CV}}$), which is used as the reference of the outer loop. In the outer loop, the real detuning ratio calculated based on (3) and (13) (i.e., $\beta_{\mathrm{Cal\_CC}}$ or $\beta_{\mathrm{Cal\_CV}}$) is employed as the feedback of the closed loop and compared with $\beta_{\mathrm{Ref\_CC}}$ or $\beta_{\mathrm{Ref\_CV}}$. Then, the difference is nullified by a PI controller. The output of the PI controller is the required duty cycle of SCC (d_{1_CC} or d_{1_CV}). The switching of charging mode can be judged by comparing the value of the real-time detuning rate with the critical detuning rate (i.e., β_{C}), as shown in Fig. 6(c). The detailed analysis is as follows. Fig. 7 presents the detuning ratio under different equivalent resistances of the battery during the charging process. It can be observed that as the equivalent resistance increases, the detuning ratio gradually decreases in CC mode, while the detuning ratio in CV

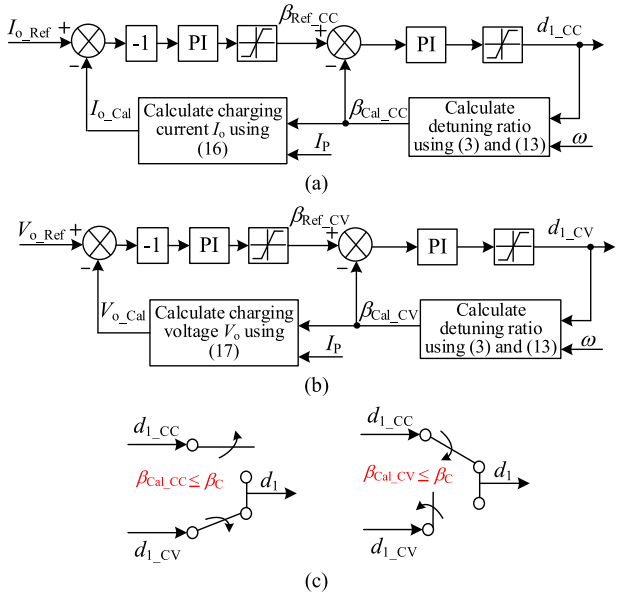

Fig. 6. Control block diagram of (a) CC charging mode, (b) CV charging mode, and (c) charging mode switching.

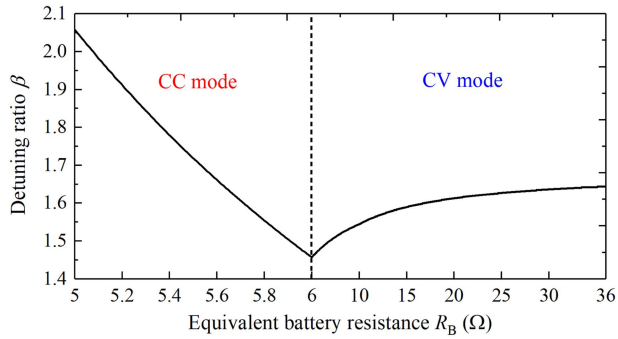

Fig. 7. Detuning ratio under different equivalent battery resistances.

mode gradually increases. Therefore, as shown in Fig. 6(c), in CC mode, when $\beta_{\mathrm{Cal\_CC}} \le \beta_{\mathrm{C}}$ is satisfied, the CC mode will be changed to CV mode. In CV mode, when $\beta_{\mathrm{Cal\_CV}} \le \beta_{\mathrm{C}}$ is satisfied, the CV mode will be changed to CC mode. The β_{C} can be calculated by submitting $I_{\mathrm{o}} = I_{\mathrm{o\_Ref}}$ and $V_{\mathrm{o}} = V_{\mathrm{o\_Ref}}$ into (16) and (17)

$$\beta_{\mathrm{C}} = \left[\frac{B + \sqrt{B^2 - \frac{32R_{\mathrm{P}}L_{\mathrm{P}}L_{\mathrm{S}}V_{\mathrm{o\_ref}}^2}{\pi^2}\left(\frac{8V_{\mathrm{o\_ref}}}{I_{0\_\mathrm{ref}}\pi^2} + R_{\mathrm{S}}\right)}}{\frac{4\sqrt{2}V_{\mathrm{o\_ref}}L_{\mathrm{P}}}{\pi}\left(\frac{8V_{\mathrm{o\_ref}}}{I_{0\_\mathrm{ref}}\pi^2} + R_{\mathrm{S}}\right)}\right]^2 \tag{21}$$

and

$$B = \frac{16\sqrt{2}V_{\mathrm{dc}}V_{0\_\mathrm{ref}}\sqrt{L_{\mathrm{P}}L_{\mathrm{S}}}}{I_{0\_\mathrm{ref}}\pi^3}. \tag{22}$$

The control flowchart of the whole charging process is presented in Fig. 8. First, the rated dc charging current $I_{\mathrm{o\_Ref}}$, the rated dc charging current $V_{\mathrm{o\_Ref}}$, and the cutoff current I_{Bmin} can be obtained based on the charging profile of the battery, and the compensation network parameters (L_{P}, L_{S}, C_{S}, C_{A}, and

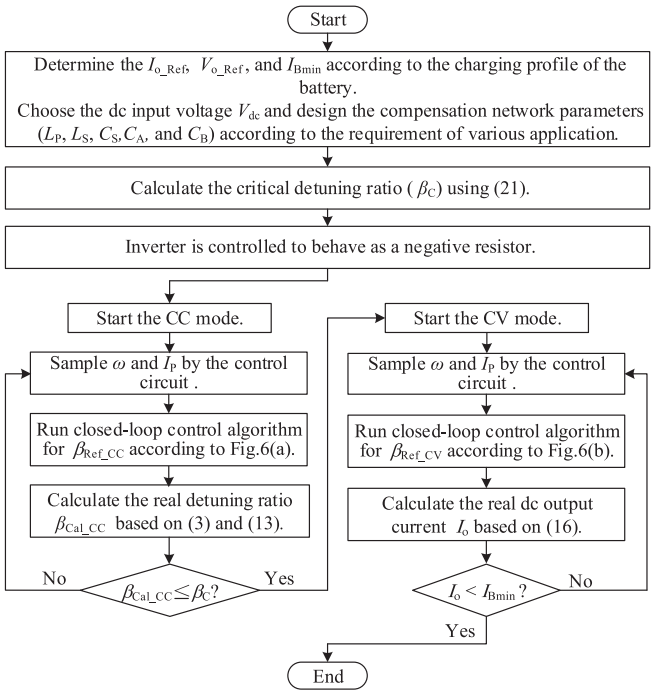

Fig. 8. Control flowchart of the whole charging process.

C_B) and the dc input voltage V_{dc} will be design in advance according to the requirement of various application. Then, the critical detuning rate β_C is calculated using (21) to determine the switching time of the charging mode. During the charging process, the inverter is controlled to behave as a negative resistor, and the CC charging mode will be activated first. In CC mode, the operation angular frequency (ω) and the transmitting current (I_P) are continuously sampled by the control circuit, and the closed-loop control algorithm for β_{Ref_CC}, as shown in Fig. 6(a), is executed to achieve constant dc output current. When $\beta_{Cal\_CC} \le \beta_C$ is satisfied, the CV charging mode is started. Similarly, based on the sampled operation angular frequency (ω) and the transmitting current (I_P), the closed-loop control algorithm for β_{Ref_CV}, as shown in Fig. 6(b), is performed to realize constant dc voltage. Finally, when the charging current I_o (the charging current I_o can be deduced using (16) without the need for receiving side information) is lower than the cutoff current I_{Bmin}, the charging process is over. It can be found that during the control process, only the operating angular frequency (ω) and the transmitting current (I_P) need to be detected. Therefore, wireless communication for real-time output regulation can be eliminated.

IV. Experimental Verifications

A. Experiment Setup

To verify the analysis and efficiency performance of the proposed system in the charging process, an experimental prototype was constructed, as shown in Fig. 9. The prototype includes a dc power source, an inverter comprised of four SiC power MOSFETs (IMW120R030M1H), a control circuit, an SS-type resonant circuit, a load-side bridge diode rectifier (DSSK80-0045B), and

TABLE I
Parameters for the Prototype

Symbol	Value	Symbol	Value
L_P	138.1 μH	V_{dc}	48 V
L_S	138.5 μH	I_{o_Ref}	6 A
R_P	0.23 Ω	V_{o_Ref}	36 V
R_S	0.21 Ω	d	5 cm
C_A	12.14 nF	$\Delta\rho$	0–6 cm
C_B	5.52 nF	k_{PS}	0.283–0.456
C_S	6.19 nF	R_B	5–6 Ω (CC mode)
β	1.457–2.058		6–36 Ω (CV mode)

an electronic load (which is used to emulate the battery). In the control circuit, a current transformer (CU8965) and a differential amplifier circuit consisting of a high-speed operational amplifier (LM6172) first convert the current signal into a voltage signal. Then, a zero-crossing detector that comprises a high-speed comparator (TL3016) is used to capture the zero-crossing point of the current i_P to generate the synchronization signal and calculate the operation frequency. Simultaneously, the root-mean-square (rms) value of i_P is measured by an rms calculator (AD637). Finally, a DSP controller (TMS320F28377D) runs the algorithm to control the inverter and SCC by the driver Si8271. The coupling coils are manufactured using the Litz wire and a ferrite layer is added behind the coils for shielding and flux guidance. The shape and size of the transmitting and receiving coils are consistent, with a dimension of 20 × 20 cm rectangle.

In the experiment, the rated charging current (I_{o_Ref}), the cutoff charging current (I_{Bmin}), the rated charging voltage (V_{o_Ref}), and the lowest charging voltage are set to be 6 A, 1 A, 36 V, and 30 V, respectively. Therefore, the equivalent resistance of the battery R_B varies within the range of 5 to 36 Ω, and the equivalent load resistance R_L can be calculated by (15). The input dc voltage is chosen to be 48 V. By submitting $I_o = I_{o\_Ref}$, $V_o = R_B I_{o\_Ref}$, and (16) into (17), the range of detuning ratio in CC mode can be deduced. Similarly, by submitting $V_o = V_{o\_Ref}$, $I_o = V_{o\_Ref} / R_B$, and (16) into (17), the reference detuning ratio of CV mode can be obtained. The transfer distance is set to be 5 cm, and the lateral misalignment $\Delta\rho$ is allowed within a range of 0–6 cm (in the experiment, the coupling coils do not move in the y-axis direction and the z-axis direction, and the different misalignment $\Delta\rho$ tests are performed by moving one of the coils parallel in the x-axis direction, as shown in Fig. 9). The corresponding coupling coefficient k_{PS} varies from 0.456 to 0.283, as shown in Fig. 10. Combined with the analysis of Section III-A, the required value of C_A and C_B can be derived. The main parameters of the prototype are given in Table I, where the value of the capacitors and coils are measured by a precision impedance analyzer (Wayne Kerr 6500B).

B. Experimental Results and Discussion

Experiments are conducted in different loading conditions and different misalignments. In the experiment, the voltages and currents are measured by the current probe (Cybertek CP0030H)

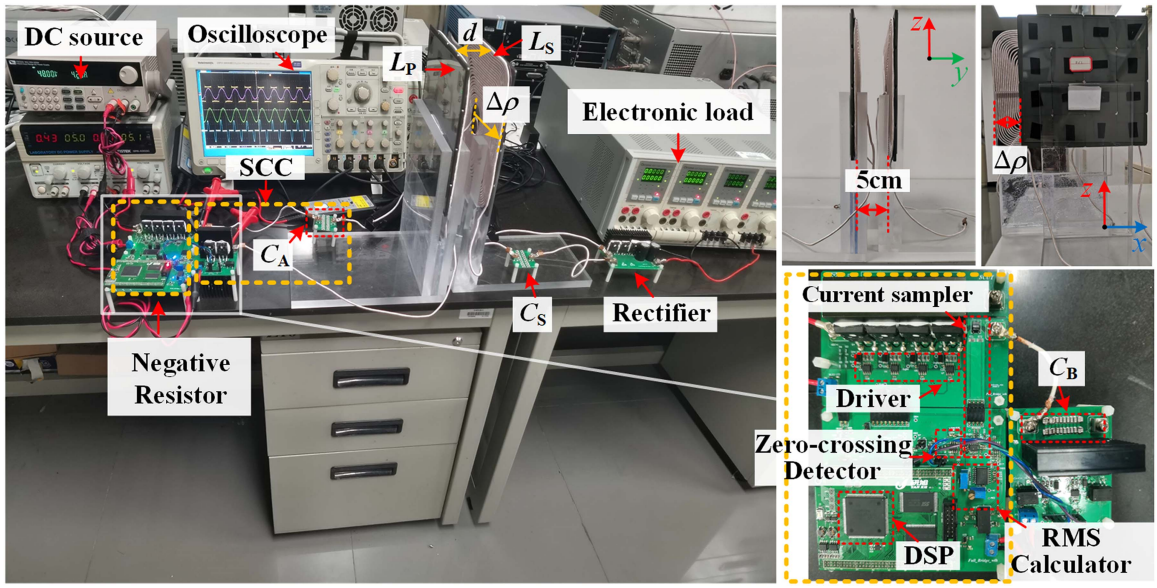

Fig. 9. Experimental prototype of the proposed system.

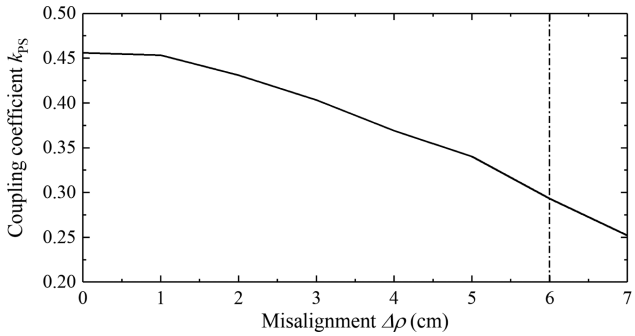

Fig. 10. Measured coupling coefficient under different lateral misalignment $\Delta\rho$.

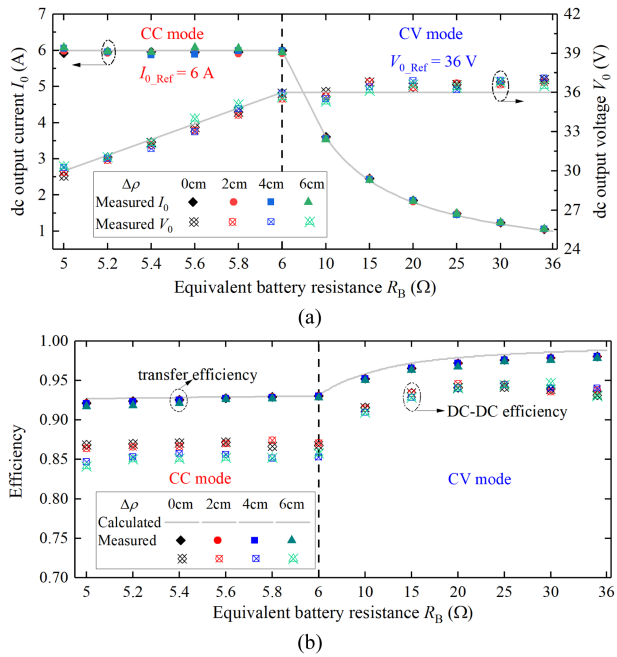

Fig. 11. Measured and calculated results. (a) Charging profile. (b) Efficiency.

and voltage probe (Cybertek P1300), and then recorded by a Tektronix Oscilloscope (Tektronix DPO 4043B). Fig. 11 shows the measured results of charging current, charging voltage, and efficiency under different misalignments. As shown in Fig. 11, constant dc output current and voltage can be achieved at different misalignments, and the charging current in CC mode and charging voltage in CV mode only vary within 1.6% and 2.2%, respectively. The transfer efficiency (coil-coil) η_T increases as the load resistance increases during the charging process and is always greater than 91.5%. The maximum dc–dc efficiency can reach 94.6%. Besides, the operation frequency of the proposed system is presented in Fig. 12. It can be found the measured operation frequencies and the calculated results are in good agreement.

Figs. 13 and 14 show the key experimental waveforms in the CC and CV modes under different load resistances and positions, respectively (from Figs. 13 and 14, the rms values of i_P, i_S, the mean values of V_o, I_o, the operation frequency, the phase relationship between v_{ac} and i_P, and the phase relationship between the voltage across SCC (v_B) and i_P under different operation conditions can be observed). It can be noted that the component of the voltage and current of the inverter is in phase during the charging process, i.e., the negative resistor can be always obtained. From Fig. 13, the dc output current can be maintained at 6 A in CC charging mode, and the constant dc output voltage can be maintained, as shown in Fig. 14. Besides, it can be also seen that when the load and coupling coefficient change, the transmitting current I_P and detuning ratio β will adaptively change. The calculated and measured results of transmitting current I_P, the detuning ratio β, and the natural frequency of transmitter and receiver under different load resistances and misalignments are presented in Fig. 15 (in theoretical calculations, the forward conduction voltage drop

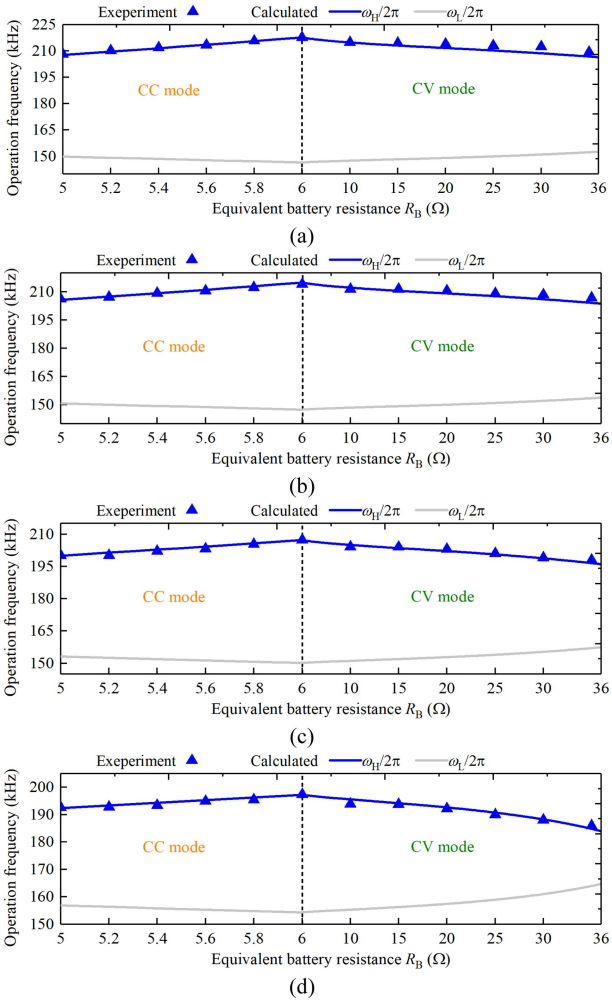

Fig. 12. Operation frequency of the proposed system. (a) $\Delta\rho = 0$ cm. (b) $\Delta\rho = 2$ cm. (c) $\Delta\rho = 4$ cm. (d) $\Delta\rho = 6$ cm.

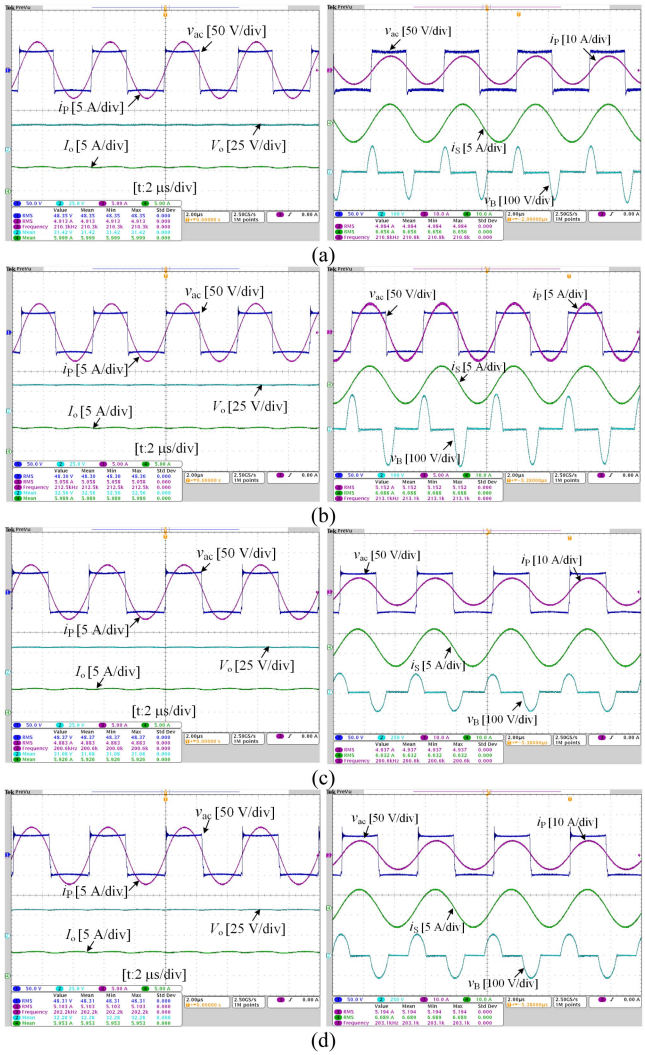

Fig. 13. Experimental waveforms in CC mode. (a) $\Delta\rho = 0$ cm, $R_B = 5.2\ \Omega$. (b) $\Delta\rho = 0$ cm, $R_B = 5.4\ \Omega$. (c) $\Delta\rho = 4$ cm, $R_B = 5.2\ \Omega$. (d) $\Delta\rho = 4$ cm, $R_B = 5.4\ \Omega$.

of Schottky rectifiers (about 0.5 V) is considered). The actual detuning ratio and natural frequency of the transmitter can be measured by DSP using (3) and (13) according to the real-time duty cycle of SCC (d_{1_CC} or d_{1_CV}) and the sampled operating angular frequency (ω). The measured results of I_P are directly obtained from the current probe and oscilloscope, and the natural frequency of the receiver is measured offline by a precision impedance analyzer. It is obvious that the measured current I_P, detuning ratio β and natural frequencies are consistent with the calculated results, which proves the correctness of the theoretical analysis.

Fig. 16 shows the detailed operation waveforms of the inverter. It can be found that the zero-phase-angle operation of the inverter can be maintained in CC and CV mode, which is beneficial for reducing the volt-ampere rating of the inverter and achieving soft switching operation. As shown in Fig. 16, when the drive signal of Q_2 ($V_{G2\text{-}3}$) arrives, the drain-source voltage of Q_2 (v_{DS_Q2}) is zero, and when Q_2 is turned OFF, the current through the Q_2 is near zero, validating the soft-switching operation can be achieved (Q_1, Q_3, and Q_4 have similar behavior). Besides, if zero-voltage switching is required, detailed parameter designs can be found in [32]. The experimental waveforms of the SCC are presented in Fig. 17, it can be observed that the drive signal of S_1 (v_{G1}) arrives when i_P commutates from negative to positive while the drive signal of S_2 (v_{G2}) becomes high level when i_P commutates from positive to negative, which agrees well with the theoretical analysis.

The dynamic performance of the proposed WPT system is tested by step changes in the load resistance R_B. From Fig. 18(a), it can be found that when R_B is changed from 5 to 5.4 Ω in CC mode, the dc output current I_o can be adjusted to the rated value 6 A within about 50 ms. Fig. 18(b) presents the dynamic waveforms in the CV mode when R_B is changed from 10 to 15 Ω. The dc output voltage can be quickly adjusted to the rated value. The dynamic adjust time is about 14 ms, and the overshoot of output voltage is 37.5 V. Besides, the CC mode can smoothly change to CV mode, as shown in Fig. 18(c).

The impact of the detuning ratio β on transfer efficiency is also tested. When $\beta = 1.45$ and $R_B = 6\ \Omega$, the experimental waveforms of the inverter output voltage v_{ac}, transmitting current

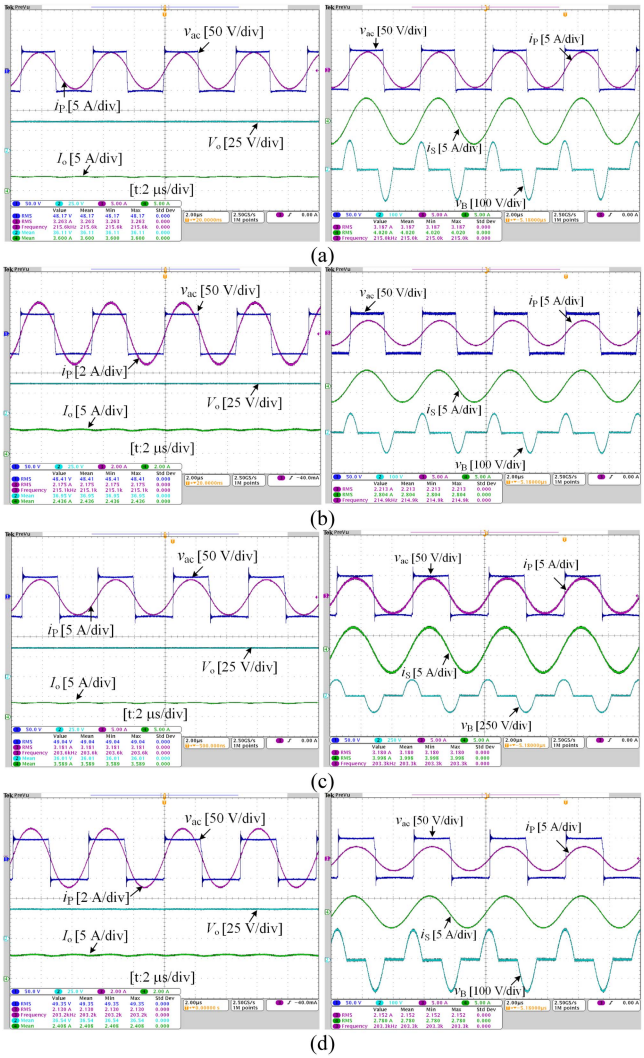

Fig. 14. Experimental waveforms in CV mode. (a) $\Delta\rho = 0$ cm, $R_B = 10\ \Omega$. (b) $\Delta\rho = 0$ cm, $R_B = 15\ \Omega$. (c) $\Delta\rho = 4$ cm, $R_B = 10\ \Omega$. (d) $\Delta\rho = 4$ cm, $R_B = 15\ \Omega$.

i_P, receiving current i_S, and the rectifier input voltage v_S under different misalignments are shown in Fig. 19. It can be found that the rms value of i_P, i_S, and v_S can be maintained constant under different misalignments, which means that a constant transfer efficiency η_T with 92.8% can be obtained when the detuning ratio is controlled to be constant (transfer efficiency is calculated by $\eta_T = I_S^2 R_L/(I_P^2 R_P + I_S^2 R_S + I_S^2 R_L)$). Fig. 20 shows the waveforms of v_{ac}, i_P, i_S, and v_S under different detuning ratios when $\Delta\rho = 0$ cm and $R_B = 6\ \Omega$. It can be found that as the detuning ratio increases, the current ratio (I_P/I_S) gradually decreases, which indicates that transfer efficiency can be improved by increasing the detuning ratio. The abovementioned experimental results are consistent with theoretical analysis.

C. Comparison With Other WPT Systems

Table II compares the performance of different WPT systems. The key parameters, including system efficiency, output power,

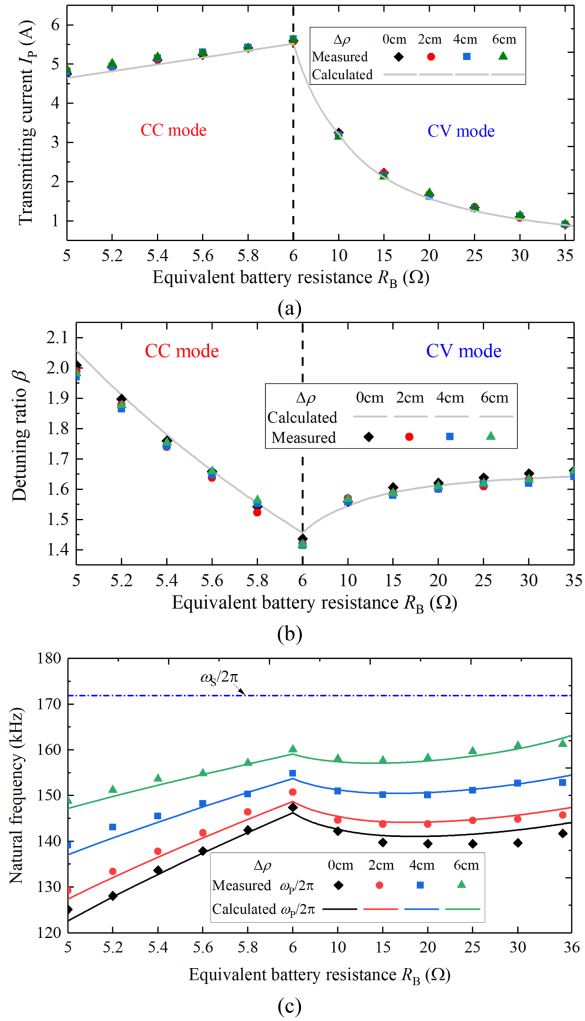

Fig. 15. Measured and calculated results. (a) Transmitting current I_P. (b) Detuning ratio. (c) Natural frequency.

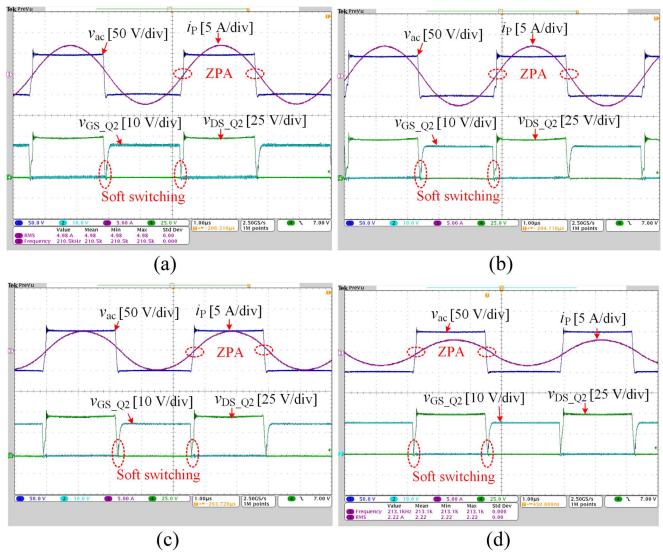

Fig. 16. Detailed Experimental operation waveforms of the inverter. (a) In CC mode: $\Delta\rho = 0$ cm, $R_B = 5.2\ \Omega$. (b) In CC mode: $\Delta\rho = 0$ cm, $R_B = 5.4\ \Omega$. (c) In CV mode: $\Delta\rho = 0$ cm, $R_B = 10\ \Omega$. (d) In CV mode: $\Delta\rho = 0$ cm, $R_B = 15\ \Omega$.

TABLE II
COMPARISONS WITH PREVIOUS WPT SYSTEMS

Ref.	Method	DC-DC efficiency	Max. output power (W)	Topologies	CC or CV	Continuously adjustable output	ZPA	Soft switching	Outputs independent of k_{PS}	Wireless communication	Extra DC-DC converter
[6]	Switching topologies	90–94.4%	1100	S-S/S-S-S	Both	No	Yes	Yes	No	Yes	No
[9]	Hybrid topologies	87–91.29 %	3000	S-LCC +S-S	CV	No	No	Yes	Quasi-constant	No	No
[19]	Frequency control	75–87%	1000	S-S	CV	No	No	Yes	Yes	Yes	No
[26]	Cascade converter	91.9%	400	S-S	No	Yes	Yes	Yes	Yes	No	Yes
[27]	Phase-shift control	72.5–95%	960	S-S	Both	Yes	Yes (CC)	No	Yes	No	No
[28]	Pulse frequency modulation	83–86.4%	40	S-S	No	No	Yes	Yes	Yes	No	No
This work	Detuning Control	84–94.6%	216	S-S	Both	Yes	Yes	Yes	Yes	No	No

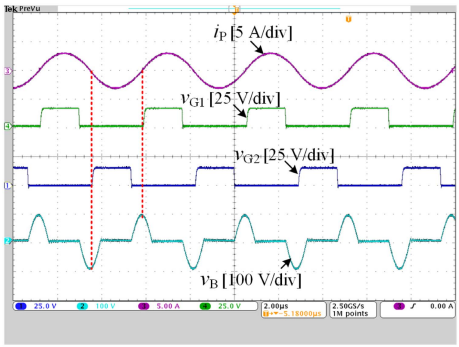

Fig. 17. Experimental waveforms of the SCC.

compensation topologies, soft switching, input and output characteristics, misalignment tolerance, output regulation ability, and additional circuits, are listed in this table. From Table II, the advantages of the proposed system are as follows.

1) Both accurate CC and CV independent of k_{PS} can be achieved. Compared to [6], the misalignment tolerance can be significantly improved. Although the outputs in [9] can remain approximately constant within a certain range of k_{PS} changes, the control accuracy of [9] is limited. And CV output and CC output cannot be realized in [9] and [19], respectively, which is not suitable for battery charging.
2) Wireless communication is not required in power transfer control, eliminating the impact of communication delays or interruptions on system dynamic response and power transmission reliability, which is an advantage compared with [6] and [19].
3) The detuning ratio increases the control freedom of the system, and the outputs can be continuously and smoothly regulated by adjusting the detuning control. The output regulation ability is enhanced compared to [6], [9], and [19]. The control accuracy is improved compared with [28] because the outputs cannot be continuously adjusted using pulse frequency modulation.

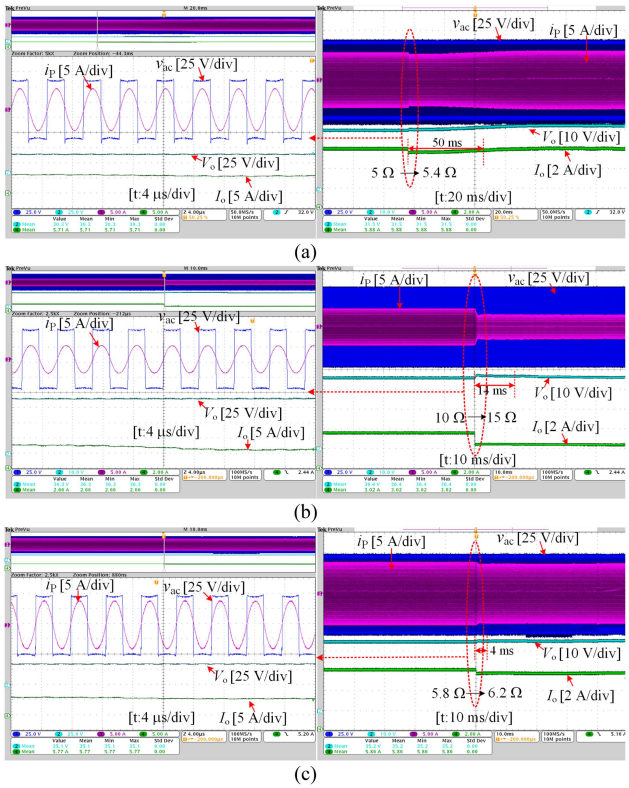

Fig. 18. Dynamic waveforms with changing R_B at $\Delta\rho = 0$ cm. (a) Changing R_B from 5 to 5.4 Ω in CC mode. (b) Changing R_B from 10 to 15 Ω in CV mode. (c) Changing from CC mode to CV mode.

4) Soft switching can be maintained because the inverter duty cycle can remain unchanged when adjusting the output, which reduces the switching loss compared to [27]. Besides, ZPA operation can be realized, which is beneficial for reducing the volt-ampere rating of the inverter compared to [6] and [19].
5) Output can be regulated by a single-stage inverter without additional dc–dc converters on both sides, which reduces the loss, cost, and volume of the system compared with

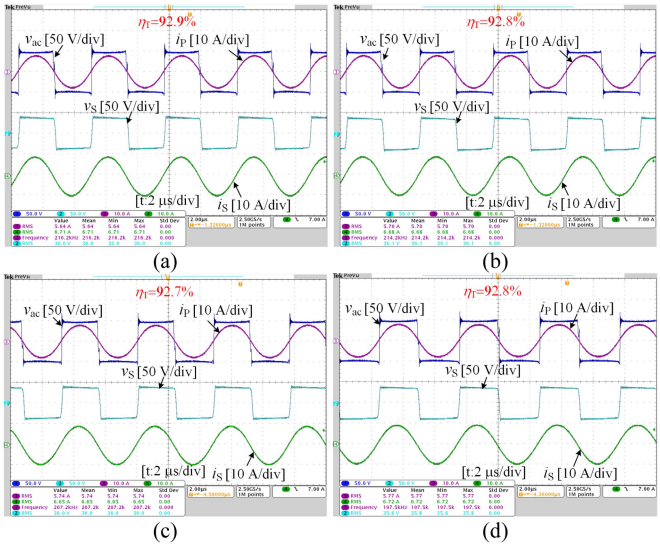

Fig. 19. Experimental waveforms of the proposed WPT system when $\beta = 1.45$ and $R_B = 6\ \Omega$ under different misalignments. (a) $\Delta\rho = 0$ cm. (b) $\Delta\rho = 2$ cm. (c) $\Delta\rho = 4$ cm. (d) $\Delta\rho = 6$ cm.

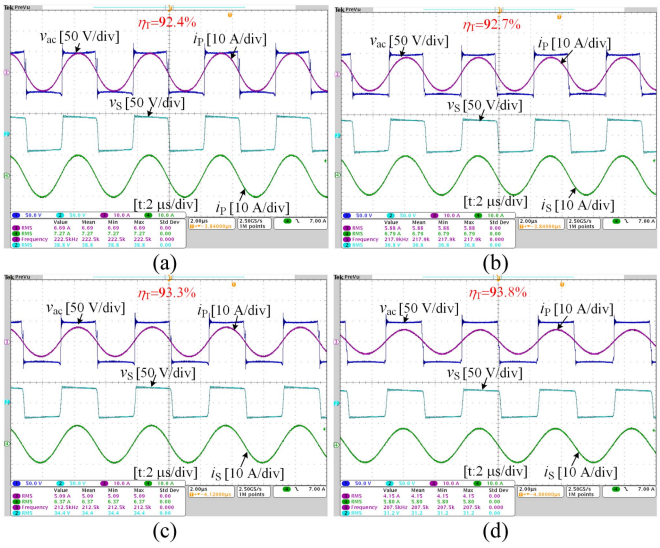

Fig. 20. Experimental waveforms of the proposed WPT system when $\Delta\rho = 0$ cm and $R_B = 6\ \Omega$ under different detuning ratios. (a) $\beta = 1.2$. (b) $\beta = 1.4$. (c) $\beta = 1.6$. (d) $\beta = 2$.

[26]. The simplest SS-type compensation topology is used, which simplifies the system structure compared to high-order compensation [9] or topology switching [6]. Thus, the requirement for a compact and lightweight system can be met.

V. Conclusion

This article proposed an autonomous WPT system for battery charging based on detuning control. First, using the circuit theory, the relationships between the detuning ratio and current ratio, voltage ratio, transfer efficiency, and output power of the proposed system were derived. Theoretical analysis demonstrates that CC and CV outputs independent of coupling coefficient and load can be achieved by controlling the detuning ratio based on the transmitting-side information. Besides, when the detuning ratio is controlled to be constant, a transfer efficiency insensitive to the variation of the coupling coefficient can be obtained, and the transfer efficiency increases as the detuning ratio increases. Next, the structure and control of the proposed system were put forward. The detailed design and implementation of the negative resistor and switching-control capacitor were presented, and a CC/CV charging control strategy with misalignment tolerance based on detuning control was also proposed. In the proposed system, wireless communication is avoided and no additional dc–dc converter is required on both sides. In the final step, a prototype with a 6-A charging current and a 36-V charging voltage was built, which was tested under different misalignments and load resistances. Experimental results show that with a transfer distance of 5 cm, CC and CV outputs can be achieved within a range of 6 cm lateral misalignment while maintaining a transfer efficiency of more than 91.5%. Besides, the charging mode can be switched smoothly, and the prototype exhibits a good dynamic response to load step changes. The experimental results confirmed the theoretical analysis.

Thereby, the proposed system can offer stronger robustness and high cost-effectiveness in wireless battery charging. Due to the use of the simplest S-type compensation structure and uncontrollable rectifier in the receiver, the proposed system has great potential for applications that require a compact and lightweight receiver, such as wireless charging for drones and smartphones.

References

[1] Z. Zhang, H. Pang, A. Georgiadis, and C. Cecati, "Wireless power transfer—An overview," *IEEE Trans. Ind. Electron.*, vol. 66, no. 2, pp. 1044–1058, Feb. 2019.

[2] C. Zhu et al., "Analysis and design of cost-effective WPT systems with dual independently regulatable outputs for automatic guided vehicles," *IEEE Trans. Power Electron.*, vol. 36, no. 6, pp. 6183–6187, Jun. 2021.

[3] M. Maier and N. Parspour, "Operation of an electrical excited synchronous machine by contactless energy transfer to the rotor," *IEEE Trans. Ind. Appl.*, vol. 54, no. 4, pp. 3217–3225, Jul./Aug. 2018.

[4] K. Song, Z. Li, J. Jiang, and C. Zhu, "Constant current/voltage charging operation for series-series and series-parallel compensated wireless power transfer systems employing primary-side controller," *IEEE Trans. Power Electron.*, vol. 33, no. 9, pp. 8065–8080, Sep. 2018.

[5] D. Maier, J. Heinrich, M. Zimmer, M. Maier, and N. Parspour, "Contribution to the system design of contactless energy transfer systems," *IEEE Trans. Ind. Appl.*, vol. 55, no. 1, pp. 316–326, Jan./Feb. 2019.

[6] Y. Zhang, Z. Shen, W. Pan, H. Wang, Y. Wu, and X. Mao, "Constant current and constant voltage charging of wireless power transfer system based on three-coil structure," *IEEE Trans. Ind. Electron.*, vol. 70, no. 1, pp. 1066–1070, Jan. 2023.

[7] M. Mohammad et al., "Bidirectional LCC–LCC-compensated 20-kW wireless power transfer system for medium-duty vehicle charging," *IEEE Trans. Transp. Electrific.*, vol. 7, no. 3, pp. 1205–1218, Sep. 2021.

[8] L. Zhao, D. J. Thrimawithana, U. K. Madawala, A. P. Hu, and C. C. Mi, "A misalignment-tolerant series-hybrid wireless EV charging system with integrated magnetics," *IEEE Trans. Power Electron.*, vol. 34, no. 2, pp. 1276–1285, Feb. 2019.

[9] W. Zhao, X. Qu, J. Lian, and C. K. Tse, "A family of hybrid IPT couplers with high tolerance to pad misalignment," *IEEE Trans. Power Electron.*, vol. 37, no. 3, pp. 3617–3625, Mar. 2022.

[10] A. Pacini, A. Costanzo, S. Aldhaher, and P. D. Mitcheson, "Load-and position-independent moving MHz WPT system based on GaN-distributed current sources," *IEEE Trans. Microw. Theory Techn.*, vol. 65, no. 12, pp. 5367–5376, Dec. 2017.

[11] N. Ha-Van and C. Seo, "Analytical and experimental investigations of omnidirectional wireless power transfer using a cubic transmitter," *IEEE Trans. Ind. Electron.*, vol. 65, no. 2, pp. 1358–1366, Feb. 2018.
[12] J. Luo et al., "Novel cuk-based bridgeless rectifier of wireless power transfer system with wide power modulation range and low current ripple," *IEEE Trans. Ind. Electron*, vol. 69, no. 3, pp. 2533–2544, Mar. 2022.
[13] M. Kim, D.-M. Joo, and B. K. Lee, "Design and control of inductive power transfer system for electric vehicles considering wide variation of output voltage and coupling coefficient," *IEEE Trans. Power Electron.*, vol. 34, no. 2, pp. 1197–1208, Feb. 2019.
[14] S. Lu, M. Böttigheimer, and N. Parspour, "An impedance mapping-based T-compensation network and control strategy for WPT system with full-bridge active rectifier," *IEEE Trans. Power Electron.*, vol. 38, no. 11, pp. 14675–14688, Jul. 2023.
[15] K. Colak, E. Asa, M. Bojarski, D. Czarkowski, and O. C. Onar, "A novel phase-shift control of semibridgeless active rectifier for wireless power transfer," *IEEE Trans. Power Electron.*, vol. 30, no. 11, pp. 6288–6297, Nov. 2015.
[16] H. Li, J. Li, K. Wang, W. Chen, and X. Yang, "A maximum efficiency point tracking control scheme for wireless power transfer systems using magnetic resonant coupling," *IEEE Trans. Power Electron.*, vol. 30, no. 7, pp. 3998–4008, Jul. 2015.
[17] X. Zhang, F. Liu, and T. Mei, "Multifrequency phase-shifted control for multiphase multiload MCR WPT system to achieve targeted power distribution and high misalignment tolerance," *IEEE Trans. Power Electron.*, vol. 36, no. 1, pp. 991–1003, Jan. 2021.
[18] U. D. Kavimandan, S. M. Mahajan, and C. W. Van Neste, "Analysis and demonstration of a dynamic ZVS angle control using a tuning capacitor in a wireless power transfer system," *IEEE Trans. Emerg. Sel. Topics Power Electron.*, vol. 9, no. 2, pp. 1876–1890, Apr. 2021.
[19] E. Gati, G. Kampitsis, and S. Manias, "Variable frequency controller for inductive power transfer in dynamic conditions," *IEEE Trans. Power Electron.*, vol. 32, no. 2, pp. 1684–1696, Feb. 2017.
[20] W. Liu, K. T. Chau, C. H. T. Lee, W. Han, X. Tian, and W. H. Lam, "Full-range soft-switching pulse frequency modulated wireless power transfer," *IEEE Trans. Power Electron.*, vol. 35, no. 6, pp. 6533–6547, Jun. 2020.
[21] J. Yin, D. Lin, T. Parisini, and S. Y. R. Hui, "Front-end monitoring of the mutual inductance and load resistance in a series–series compensated wireless power transfer system," *IEEE Trans. Power Electron.*, vol. 31, no. 10, pp. 7339–7352, Oct. 2016.
[22] Y. Yang, S. C. Tan, and S. Y. R. Hui, "Fast hardware approach to determining mutual coupling of series–Series-compensated wireless power transfer systems with active rectifiers," *IEEE Trans. Power Electron.*, vol. 35, no. 10, pp. 11026–11038, Oct. 2020.
[23] S. Assawaworrarit, X. Yu, and S. Fan, "Robust wireless power transfer using a nonlinear parity-time-symmetric circuit," *Nature*, vol. 546, no. 7658, pp. 387–390, Jun. 2017.
[24] J. Zhou, B. Zhang, W. Xiao, D. Qiu, and Y. Chen, "Nonlinear parity-time-symmetric model for constant efficiency wireless power transfer:Application to a drone-in-flight wireless charging platform," *IEEE Trans.Ind. Electron.*, vol. 66, no. 5, pp. 4097–4107, May 2019.
[25] Y. Jiang and B. Zhang, "A fractional-order wireless power transfer system insensitive to resonant frequency," *IEEE Trans. Power Electron.*, vol. 35, no. 5, pp. 5496–5505, May 2020.
[26] H. Zhu, B. Zhang, and L. Wu, "Output power stabilization for wireless power transfer system employing primary-side-only control," *IEEE Access*, vol. 8, pp. 63735–63747, 2020.
[27] L. Wu, B. Zhang, and Y. Jiang, "Position-independent constant current or constant voltage wireless electric vehicles charging system without dual-side communication and DC–DC converter," *IEEE Trans. Ind. Electron.*, vol. 69, no. 8, pp. 7930–7939, Aug. 2022.
[28] Z. Hua, K. T. Chau, W. Liu, and X. Tian, "Autonomous pulse frequency modulation for wireless battery charging with zero-voltage switching," *IEEE Trans. Ind. Electron.*, vol. 70, no. 9, pp. 8959–8969, Sep. 2023.
[29] A. E. Aroudi, J. Huang, M. S. Al-Numay, and L. Zhen, "On the coexistence of multiple limit cycles in H-bridge wireless power transfer systems with zero current switching control," *IEEE Trans. Circuits Syst. I, Reg. Papers*, vol. 67, no. 5, pp. 1729–1739, May 2020.
[30] S. Assawaworrarit and S. Fan, "Robust and efficient WPT using a switch-mode implementation of a nonlinear parity-time symmetric circuit," *Nature Electron.*, vol. 546, no. 7658, pp. 387–390, Apr. 2020.
[31] P. Tan, B. Song, W. Lei, Y. Han, and B. Zhang, "Decoupling control of double-side frequency tuning for LCC/S WPT system," *IEEE Trans. Ind. Electron.*, vol. 70, no. 11, pp. 11163–11173, Nov. 2023.
[32] S. Sun, B. Zhang, C. Rong, X. Shu, and Z. Wei, "A multireceiver wireless power transfer system using self-oscillating source composed of zero-voltage switching full-bridge inverter," *IEEE Trans. Indust. Electron.*, vol. 69, no. 3, pp. 2885–2895, Mar. 2022.

Lihao Wu was born in Fujian, China, in 1994. He received the B.S. degree in electrical engineering from Fuzhou University, Fuzhou, China, in 2017, and the Ph.D. degree in power electronics from the School of Electric Power, South China University of Technology, Guangzhou, China, in 2022.

His research interests include wireless power transfer applications and power electronics converters.

Bo Zhang (Fellow, IEEE) was born in Shanghai, China, in 1962. He received the B.S. degree in electrical engineering from Zhejiang University, Hangzhou, China, in 1982, the M.S. degree in power electronics from Southwest Jiaotong University, Chengdu, China, in 1988, and the Ph.D. degree in power electronics from the Nanjing University of Aeronautics and Astronautics, Nanjing, China, in 1994.

He is currently a Professor with the School of Electric Power, South China University of Technology, Guangzhou, China. He has authored or coauthored seven books in IEEE–Wiley and Springer and more than 600 technical papers, and he holds more than 230 patents. His current research interests include nonlinear analysis, modeling and control of power electronic converters, and wireless power transfer applications.

Yanwei Jiang (Member, IEEE) received the B.S. degree in electrical engineering and M.S. degree in control theory and control engineering from Fuzhou University, Fuzhou, China, in 2012 and 2015, respectively, and the Ph.D. degree in power electronics at School of Electric Power, South China University of Technology, Guangzhou, China, in 2019.

His research interests include wireless power transfer applications, power electronics converters, and fractional-order systems.